

Grain Alignment and Dust Evolution Physics with Polarisation (GRADE-POL)

I. Dust Polarisation Modelling for Isolated Starless Cores

Le Ngoc Tram^{1,2*}, Thiem Hoang^{3,4}, Alex Lazarian⁵, Daniel Seifried⁶, B-G Andersson⁷, Thushara G.S. Pillai⁸, Bao Truong³, Pham Ngoc Diep^{9,10}, Lapo Fanciullo¹¹

¹ Leiden Observatory, Leiden University, PO Box 9513, 2300 RA Leiden, The Netherlands

² Max-Planck-Institut für Radioastronomie, Auf dem Hügel 69, 53121, Bonn, Germany

³ Korea Astronomy and Space Science Institute, Daejeon 34055, Republic of Korea

⁴ Department of Astronomy and Space Science, University of Science and Technology, 217 Gajeong-ro, Yuseong-gu, Daejeon, 34113, Republic of Korea

⁵ Department of Astronomy, University of Wisconsin-Madison, Madison, WI, 53706, USA

⁶ I. Physikalisches Institut, Universität zu Köln, Zùlpicher Str. 77, D-50937 Köln, Germany

⁷ McDonald Observatory, University of Texas at Austin, 2515 Speedway Boulevard, Austin, TX 78712, USA

⁸ Haystack Observatory, Massachusetts Institute of Technology, 99 Millstone Road, Westford, MA 01886, USA

⁹ Department of Astrophysics, Vietnam National Space Center, Vietnam Academy of Science and Technology, 18 Hoang Quoc Viet, Hanoi, Vietnam

¹⁰ Graduate University of Science and Technology, Vietnam Academy of Science and Technology, 18 Hoang Quoc Viet, Hanoi, Vietnam

¹¹ National Chung Hsing University, 145 Xingda Rd., South Dist., Taichung City 402, Taiwan

January 28, 2025

ABSTRACT

The polarisation of light induced by aligned interstellar dust serves as a significant tool in investigating cosmic magnetic fields, dust properties, and poses a challenge in characterising the polarisation of the cosmic microwave background and other sources. To establish dust polarisation as a reliable tool, the physics of the grain alignment process needs to be studied thoroughly. The Magnetically enhanced Radiative Torque (MRAT) alignment is the only mechanism that can induce highly efficient alignment of grains with magnetic fields required by polarisation observations of the diffuse interstellar medium. Here, we aim to test the MRAT mechanism in starless cores using the multiwavelength polarisation from optical/NIR to far-IR/submm. Our numerical modelling of dust polarisation using the MRAT theory demonstrated that the alignment efficiency of starlight polarisation (p_{ext}/A_V) and the degree of thermal dust polarisation (p_{em}) first decrease slowly with increasing visual extinction (A_V) and then falls steeply as $\propto A_V^{-1}$ at large A_V due to the loss of grain alignment, which explains the phenomenon known as polarisation holes. Visual extinction at the transition from shallow to steep slope (A_V^{loss}) increases with the maximum grain size. By applying physical profiles suitable for a starless core 109 in the Pipe Nebula (Pipe-109), our model successfully reproduces the existing observations of starlight polarisation at R-band ($0.65 \mu\text{m}$) and H-band ($1.65 \mu\text{m}$), as well as emission polarisation at submillimeter ($850 \mu\text{m}$). Successful modelling of observational data requires perfect alignment of large grains as evidence of the MRAT mechanism, and larger maximum size with higher elongation at higher A_V . The latter reveals the first evidence for the new model of anisotropic grain growth induced by magnetic grain alignment. This paper introduces the framework to probe the fundamental physics of grain alignment and dust evolution using multi-wavelength dust polarisation (GRADE-POL) and is the first of our GRADE-POL series.

Key words. ISM: dust, extinction – ISM: clouds – Infrared: ISM – Submillimeter: ISM – Radiative transfer, Polarisation

1. Introduction

The polarisation of starlight and dust emission caused by alignment of dust grains (hereafter dust polarisation) is commonly used to detect magnetic fields in the interstellar medium of our galaxy (e.g. [Pattle et al. 2023](#)) and external galaxies, both nearby (e.g. [Borlaff et al. 2023](#)) and far away (e.g. [Geach et al. 2023](#)). It also presents a challenge as a foreground contamination for characterising the cosmic microwave background (e.g. [Planck Collaboration et al. 2020](#)), exoplanetary atmospheres (e.g. [van](#)

[Holstein et al. 2021](#)) and other sources. Hence, a thorough understanding of the physical processes behind dust polarisation and grain alignment is necessary.

After detections of the extinction (starlight) polarisation ([Hall 1949](#); [Hiltner 1949](#)) and emission (thermal dust) polarisation ([Cudlip et al. 1982](#)), numerous studies have been carried out to establish a theory for the physics of grain alignment. The alignment by radiative torques (RATS), which was initially proposed by [Dolginov & Mitrofanov \(1976\)](#), has been widely accepted as a leading theory of grain alignment. This RAT idea was supported by numerical simulations in [Draine & Weingartner \(1996\)](#). Then, the rotation of dust grains exposed to a laser

* Corresponding author: Le Ngoc Tram
e-mail: nle@strw.leidenuniv.nl, nle@mpi-fr-bonn.mpg.de

beam has been observed in the laboratory experiment (Abbas et al. 2004). A simple analytical model for helical grains in Lazarian & Hoang (2007) and numerical calculations in Hoang & Lazarian (2008) allowed efficient exploration of the parameter space of the dynamics of dust grains subjected to radiation. These analytical and numerical studies showed that the fraction of grains that can be aligned at an attractor point with high angular momentum J (called high- J attractors) by RATs strongly varies with the angle between the radiation and interstellar magnetic field directions. This angle dependence has also been reported from observations in Andersson et al. (2011). Comprehensive studies on RAT alignment for a large sample of grain shapes were presented in Herranen et al. (2019, 2021). For the ensemble of shapes considered in Herranen et al. 2021, on average, only about 20 – 40% of the grains can be aligned at high- J attractors by RAT for a typical interstellar radiation field (ISRF; see their Figure 5).

For grains with embedded iron inclusions, the effect of magnetic relaxation cannot be ignored in the consideration of RAT alignment. The theoretical study in Lazarian & Hoang (2008) shows that the enhancement in magnetic susceptibility due to iron inclusions could increase the fraction of grains aligned at high- J attractors. For example, for a small magnetic inclusion, about 70% of the grains can align at high- J attractors, and a considerable iron inclusion can allow 100% of grains to align at high- J attractor for the same ISRF (see Hoang & Lazarian 2016, also Figure 10 in Herranen et al. 2021). In particular, numerical calculations in Hoang & Lazarian (2016) showed that grains could be perfectly aligned by a magnetically enhanced RAT (aka MRAT) mechanism. We note that the classical RAT theory has been shown to qualitatively reproduce dust polarisation observations from diffuse to molecular clouds (see a review in Andersson et al. 2015). However, a quantitative comparison between theoretical modelling and Planck observational data reveals the need for highly efficient grain alignment in the diffuse ISM (Hensley & Draine 2023) and molecular clouds (Reissl et al. 2020), which requires the MRAT mechanism. In particular, the high polarisation up to 30 – 40% observed in dense protostellar environments by ALMA provides strong support for the MRAT mechanism (Giang et al. 2023; Giang & Hoang 2024; Thang et al. 2024; Giang et al. 2024). In this paper, we will seek evidence of the MRAT in dense starless cores, which are the intermediate structures between MCs and protostellar cores.

The continuous development of the RAT alignment theory (Hoang et al. 2019; Hoang & Tram 2020) demonstrated that in the presence of a strong radiation field, large dust grains rotating at high- J attractors can achieve an exceptionally high angular velocity. These grains will spontaneously be disrupted into smaller fragments as soon as the centrifugal force within the grain exceeds the binding force that holds it together. This effect of rotational disruption is termed Radiative Torque Disruption (RAT-D). Laboratory experiments have shown extremely rapid rotation of objects due to laser irradiation (e.g. Reimann et al. 2018; Ahn et al. 2018), and the disruptive impact of rotation is also observed in simulations (Reissl et al. 2023) and laboratory experiments (Holgate et al. 2019). The combination of the RAT alignment with the RAT-D mechanisms constitutes the RAT paradigm, which has been shown to account for a wider range of dust polarisation towards star-forming regions (see a review in Tram & Hoang 2022). Thus, the RAT paradigm has been demonstrated to be a foundational framework to describe grain alignment and grain disruption driven by radiation.

To extend the application of the RAT paradigm in various astrophysical environments, we developed a physical (forward)

model to predict the degree of polarisation at multiple wavelengths for both dichroic extinction (starlight polarisation, p_{ext}) and thermal dust polarisation (emission polarisation, p_{em}). This physical model is based on the alignment degree predicted by the RAT paradigm, but it assumes uniform magnetic fields and neglects the depolarisation owing to fluctuations of the magnetic field, as well as excluding the radiative transfer process. The model is coded in PYTHON and is described in Lee et al. (2020) and Tram et al. (2021a). We now name this code as DUSTPOL-PY¹. Despite simplicity, DUSTPOL-PY was shown to be able to reproduce the relation of p_{em} with the temperature of the dust (a proxy of radiation intensity) in star-forming regions, averaging over the cloud (Lee et al. 2020; Tram et al. 2021a,b) and on a map (pixel-by-pixel, Ngoc et al. 2024). This model was also shown to reproduce the spectrum of thermal dust polarisation, from 54 to 850 μm in the OMC-1 cloud (Tram et al. 2024). In these early investigations, the model was treated as zero dimensional and included local physical parameters such as the gas volume density and the dust temperature, which were derived from observational data. Furthermore, the model’s ability to predict starlight polarisation has not been thoroughly utilised.

Another longstanding problem in dust astrophysics is how dust grains grow in the ISM and dense molecular clouds. It is well known that grains can grow by gas accretion and grain-grain collisions, but the detailed physics is unclear. Traditionally, grain growth is usually assumed to be isotropic because of the random motion of gas and grains, which results only in the increase in the grain size (see, e.g., Hirashita & Li 2013), but the evolution of grain shape during grain growth is not yet studied in detail. Therefore, some authors suggest that grain growth would make big grains to become spherical and thus reduces the dust polarization efficiency, which might explain the polarization hole (Weintraub et al. 2000; Gupta et al. 2024). However, such a suggestion is in conflict with high polarization degree of starlight and dust emission in dense protostellar cores observed by ALMA where grain growth is most efficient. A recent theoretical study in Hoang (2022) revealed two new effects of grain alignment on grain growth. First, the growth of aligned grains as a result of gas accretion becomes anisotropic due to the alignment of grains with the magnetic field. This results in an increase in grain elongation during the grain growth process. Second, grain growth by coagulation due to collisions between aligned grains results in the formation of composite grains that have elongation increasing with grain growth. Polarisation is a unique tool to constrain both grain size and shape, as shown in the pioneering study for the ISM by Draine (2024). Nevertheless, the shape of dust grains and its effect on dust polarisation in dense clouds where grain growth is most efficient are not well studied. Compared to the prolate shape of the grain, the oblate grains are shown to fit better to the observed mid-infrared polarisation to Orion/Becklin–Neugebauer (Aitken et al. 1989) and to the Chamaeleon I cloud (Andersson & Potter 2010; Andersson et al. 2011). However, Draine & Hensley (2021) showed that both prolate and oblate grains could reproduce the mid-infrared polarisation towards two lines of sight of the diffuse ISM presented in Wright et al. (2002). Very recently, Reissl et al. (2024) showed that the fast rotation of the grain and the resulting centrifugal force can cause grains to have oblate shapes, with the elongation increasing with the rotation rate. Since RATs cause grain alignment and suprathreshold rotation, it implies that RATs

¹ Github: <https://github.com/lengoctram/DustPOL-py>
Manual website: <https://lengoctram.github.io/DustPOL-website/>
Interactive website: <https://dustpol-py.streamlit.app>

are also important for the evolution of grains in size (growth and disruption) and shapes (oblate and elongation).

In this work, our objective is to constrain the grain alignment and dust evolution physics using dust polarisation (GRADE-POL). Toward this goal, we improve our DUSTPOL-PY code and apply it to isolated starless spherical cores. Note that starless cores are an ideal target for our study because of the high density at which grain growth is expected to occur, and grain alignment is still significant. Numerous starless cores have been observed in multiple wavelengths from starlight polarisation in optical and near-infrared (Near-IR) to thermal dust polarisation in the submillimeter (submillimeter) range. These observations usually report a drop of p_{ext}/A_V and/or p_{em} from the cloud surface to the core via the relation to the total intensity (I) or visual extinction (A_V) as a power law ($p_{\text{ext}}/A_V \sim A_V^{-\alpha}$ or $p_{\text{em}} \sim A_V^{-\alpha}$) (see, e.g. Gerakines et al. 1995; Whittet et al. 2008; Alves et al. 2014; Hull et al. 2014). In some cases, this slope α approaches 1 in close proximity to the centre of the cores (Jones et al. 2015), which is known as the polarisation hole.

Note that earlier studies have attempted to interpret observed dust polarisation in starless cores, using the original classical RAT theory from Lazarian & Hoang (2007), for starlight polarisation (Whittet et al. 2008; Hoang et al. 2015) and thermal dust polarisation (Cho & Lazarian 2005; Bethell et al. 2007). Most recently, based on the RAT paradigm, the theoretical work in Hoang et al. (2021), with a simple radiative transfer consideration, explained that the slope of $p_{\text{em}} \sim A_V^{-1}$ could be a result of loss of aligned grain and predicted that the $p_{\text{em}} - A_V$ relation could be used to investigate grain growth in starless cores. In this paper, we will model simultaneously the multiwavelength polarisation of starlight and thermal dust emission using the state-of-the-art RAT paradigm and compare it with the observational data.

In our previous research, we explored three scenarios for dust grain population: separated silicate and carbonaceous particles, or mixed composition. Specifically, using multiple wavelengths of thermal dust polarisation in Tram et al. (2024), we demonstrated that a combined composition of carbonaceous and silicate (bonded together) is necessary to understand the observations towards the Orion molecular cloud. This mixture leads to a flat polarisation spectrum in the submillimeter range because of the slightly different temperatures of the silicate and carbonaceous grains. This characteristic is similar to the new model of composite cosmic dust (ASTRODUST) introduced by Hensley & Draine (2023), which effectively reproduces the flat spectrum seen by Planck and the BlastPOL balloon. Note that the composite interstellar dust was first proposed in Mathis & Whiffen (1989); Tielens (1989). In addition, numerical simulation in Reissl et al. (2023) showed that a rotating grain is likely to have an oblate shape. In this work, we will incorporate and only consider the oblate ASTRODUST composition.

This paper is structured as follows. We summarise the fundamental mathematical formalism for the physical properties of starless cores and alignment by RATs used in DUSTPOL-PY in Section 2. Section 3 shows the numerical results. We discuss our results in Section 4, in which we model the multiwavelength polarisation and compare it to observations for a particular case of the Pipe-109 starless core in optical, Near-IR, and submillimeter wavelengths. The conclusion is given in Section 5.

2. Model Formalism

Here, we first review the foundational formulations and physical parameters that underlie our model, including the astrophys-

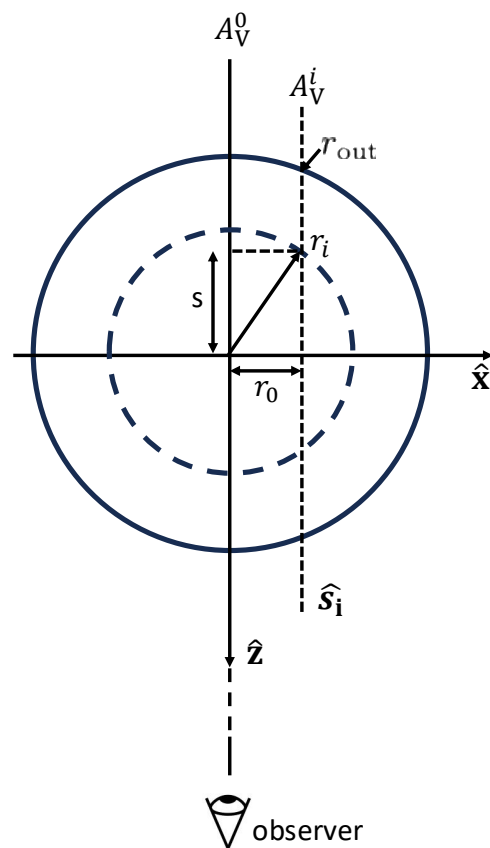


Fig. 1: Coordinate system of the starless core on the (x, z) -plane with the \hat{z} direction towards the observer. The position in the plane of the sky is defined by r_0 . Each line of sight \hat{s} corresponds to a distinct visual extinction A_V , calculated due to the gas volume density profile along this direction. At a location r_i on the sight line, the physical parameters (such as gas density, temperature, and radiation field) are the same on the dashed circle.

ical object and dust alignment. For the dust model, we consider the optical constants of the new ASTRODUST (Hensley & Draine 2023).

2.1. Numerical setup

This work aims at starless cores (or dense clouds), which are assumed to have a spherical geometry of a radius of r_{out} (see Figure 1). The line of sight follows the \hat{z} direction in Cartesian coordinates.

Calculations are carried out on the $\hat{x}\hat{z}$ plane with $y = 0$ (the largest circular slice). We sample 37 values of r_0 from 0 to r_{out} , and 70 values of s from $-r_{\text{out}}$ to r_{out} . These samplings are in linear space. For a given line of sight (\hat{s}_i with a projected distance to the centre of the core of r_0), the radial distance along this line of sight is $r_i = \pm \sqrt{s^2 + r_0^2}$ with $|s|$ varying from $-r_{\text{out}}$ to r_{out} . Due to the assumption of spherical symmetry of the starless core, the calculation is not executed for $r_i > r_{\text{out}}$.

For each line of sight with the position r_0 , the visual extinction A_V^i observed by the observer is calculated as

$$A_V(r_0) = 1.086\tau_{0.55\mu\text{m}}(r_0) \quad (1)$$

with the optical depth as

$$\tau_{0.55\mu\text{m}}(r_0) = \int_s n_{\text{H}} ds \left(\int_{a_{\text{min}}}^{a_{\text{max}}} \pi a^2 Q_{\text{ext},0.55\mu\text{m}}(a) \frac{1}{n_{\text{H}}} \frac{dn}{da} da \right) \quad (2)$$

where Q_{ext} is the extinction efficiencies of the dust grain, and dn/da is the grain size distribution. For a given grain size distribution, visual extinction is sensitive to the chosen maximum grain size, e.g., a smaller a_{max} results in higher A_{V} . We did not model the evolution of grain size within the cores.

2.2. Physical profiles

This section outlines the parametric expressions for the physical profiles applied in our model. We refer to [Hoang et al. \(2021\)](#) for the origins and detailed derivations.

2.2.1. Gas density and attenuation

We consider a typical model of starless cores with a flat central peak and a decreasing gas density outward. Let n_0 be the gas density in the central region and r be the radial distance from the centre. The density profile can be described by

$$n_{\text{H}}(r) = \begin{cases} n_0 & \text{for } r \leq r_{\text{flat}}, \\ n_0 \left(\frac{r}{r_{\text{flat}}}\right)^{-\alpha} & \text{for } r > r_{\text{flat}}, \end{cases} \quad (3)$$

where r extends to r_{out} , making n_0 , r_{out} , r_{flat} , and α parameters within our model. In this work, we only consider the particular case of $\alpha = 2$ as in [Whitworth & Ward-Thompson \(2001\)](#). The other three parameters are adjusted from the observational constraints, e.g. gas volume density or visual extinction. The case with $\alpha = 0$ corresponds to a uniform molecular cloud.

The gas column density (N_{H}) integrated from the center to the position r in the envelope along the radial distance, and the corresponding visual extinction ($A_{\text{V}}^{\text{outward}}$) are

$$N_{\text{H}}(r) = \int_0^r n_{\text{H}}(r') dr' \quad (\text{cm}^{-2})$$

$$A_{\text{V}}^{\text{outward}} = \left(\frac{N_{\text{H}}}{5.8 \times 10^{21} \text{ cm}^{-2}} \right) R_{\text{V}} \quad (\text{mag}) \quad (4)$$

where R_{V} is the total-to-selective extinction ratio. We adopt $R_{\text{V}} = 4$ to account for the larger grains compared to the typical interstellar medium. The visual extinction ($A_{\text{V}}^{\text{ext}}$) measured from the envelope to the centre is expressed as

$$A_{\text{V}}^{\text{ext}} = A_{\text{V}}^{\text{outward}}(r \gg r_{\text{flat}}) - A_{\text{V}}^{\text{outward}}(r)$$

$$= 10.3 \left(\frac{n_0}{10^8 \text{ cm}^{-3}} \right) \left(\frac{r_{\text{flat}}}{10 \text{ au}} \right) \left(\frac{R_{\text{V}}}{4} \right) \times \begin{cases} \left(\frac{\alpha}{\alpha-1} - \frac{r}{r_{\text{flat}}} \right) & \text{for } r \leq r_{\text{flat}} \\ \frac{1}{\alpha-1} \left(\frac{r}{r_{\text{flat}}} \right)^{1-\alpha} & \text{for } r > r_{\text{flat}} \end{cases} \quad (5)$$

It is worth noticing that this visual extinction differs from the line of sight A_{V} in Equation 1.

2.2.2. Radiation field and grain temperature

Due to the lack of embedded internal radiation sources within a starless core, the local radiation field inside the starless core is just an attenuated interstellar radiation field (ISRF). Let u_{rad} be the radiation energy density, and U be the strength of the local radiation field, defined as $U = u_{\text{rad}}/u_{\text{MMP}}$ with $u_{\text{MMP}} = 8.64 \times 10^{-13} \text{ erg cm}^{-3}$ is the energy density of the local radiation

field in the solar neighborhood ([Mathis et al. 1983](#)). Following numerical calculations in [Hoang et al. \(2021\)](#), where they fitted empirical functions to the results of radiative transfer calculations, the strength of the attenuated ISRF at a visual extinction $A_{\text{V}}^{\text{ext}}$ inside a starless core is parameterized as

$$U(A_{\text{V}}^{\text{ext}}) = \frac{\int_0^{\infty} u_{\lambda}(A_{\text{V}}^{\text{ext}}) d\lambda}{u_{\text{MMP}}} = \frac{U_0}{1 + 0.42 \times (A_{\text{V}}^{\text{ext}})^{1.22}}. \quad (6)$$

where u_{λ} is the specific radiation energy density in the units of erg cm^{-4} . U_0 is the radiation strength measured on the cloud surface, which is assumed to be the same as the diffuse ISRF. For a typical ISRF in the solar neighborhood ([Mathis et al. 1983](#)), $U_0 = 1$, but a recent study suggests $U_0 = 1.5$ ([Bianchi 2024](#)).

The corresponding mean wavelength of the ISRF is

$$\bar{\lambda}(A_{\text{V}}^{\text{ext}}) = \frac{\int_0^{\infty} \lambda u_{\lambda}(A_{\text{V}}^{\text{ext}}) d\lambda}{\int_0^{\infty} u_{\lambda}(A_{\text{V}}^{\text{ext}}) d\lambda} = \bar{\lambda}_0 \left[1 + 0.27 \times (A_{\text{V}}^{\text{ext}})^{0.76} \right] \quad (7)$$

where $\bar{\lambda}_0$ is the mean wavelength of the ISRF at the cloud surface, and for the typical ISRF, $\bar{\lambda}_0 = 1.2 \mu\text{m}$.

In dense and cold environments such as starless cores, gas and dust are in thermal equilibrium, i.e., $T_{\text{gas}} = T_{\text{dust}}$. Therefore, one can determine the gas and dust temperatures using the radiation strength given by Eq. 6 using the formula from [Draine \(2011\)](#):

$$T_{\text{d}}(A_{\text{V}}^{\text{ext}}) = T_{\text{gas}}(A_{\text{V}}^{\text{ext}}) = 16.4 \text{ K} \times \left(\frac{a}{0.1 \mu\text{m}} \right)^{-1/15} \left[U(A_{\text{V}}^{\text{ext}}) \right]^{1/6}. \quad (8)$$

2.2.3. Grain size distribution

We make use of the well-known MRN-like grain size distribution with $dn/da \sim Ca^{-\beta}$, the normalisation factor C is estimated by the mass conversion as ([Tram et al. 2020, 2021a](#))

$$C = \frac{(4 + \beta) M_{\text{d/g}} m_{\text{gas}}}{\frac{4}{3} \pi \rho_{\text{dust}} (a_{\text{max}}^{4+\beta} - a_{\text{min}}^{4+\beta})} \quad \text{for } \beta \neq -4$$

$$C = \frac{M_{\text{d/g}} m_{\text{gas}}}{\frac{4}{3} \pi \rho_{\text{dust}} (\ln a_{\text{max}} - \ln a_{\text{min}})} \quad \text{for } \beta = -4 \quad (9)$$

where $M_{\text{d/g}}$ is the dust-to-gas mass ratio ($M_{\text{d/g}} = 0.01$ for a typical ISM), ρ_{dust} is the mass density of dust ($\rho_{\text{dust}} = 2.71 \text{ g cm}^{-3}$ for [ASTRODUST](#) with the porosity of 20% ([Hensley & Draine 2023](#)), $m_{\text{gas}} = \mu m_{\text{H}}$ is the mean molecular gas mass per hydrogen atom (we use $\mu = 2.8$ for molecular gas). Note that this normalisation factor establishes the value of the line-of-sight extinction A_{V} , but cancels out when considering the starlight polarisation to extinction ($p_{\text{ext}}/A_{\text{V}}$ – mostly used in observations), as well as the thermal dust polarisation p_{em} . In contrast, the power law of the distribution exerts a significant influence.

2.3. Grain Alignment by the Radiative Torque Paradigm

The physics of grain alignment by radiative torques is described in detail in numerous works. In this section, we restate the principles of this theory and formulations for our model. For more details, we refer to the most recent reviews in [Andersson et al. \(2015\)](#); [Tram & Hoang \(2022\)](#) and studies in [Lazarian & Hoang \(2021\)](#); [Hoang et al. \(2022\)](#).

2.3.1. Radiative Torques

The average radiative torque induced by the interaction of an irregular grain (with an effective size a), and an anisotropic radiation field (with an isotropic degree of γ) is

$$\bar{\Gamma}_{\text{RAT}} = \pi a^2 \gamma u_{\text{rad}} \left(\frac{\bar{\lambda}}{2\pi} \right) \bar{Q}_{\Gamma} \quad (10)$$

where $u_{\text{rad}} = U u_{\text{MMP}}$ is the energy density of the local radiation field, and \bar{Q}_{Γ} is the RAT efficiency given by

$$\bar{Q}_{\Gamma} = \begin{cases} 2 \left(\frac{\bar{\lambda}}{a} \right)^{-2.7} & \text{for } a \leq \frac{\bar{\lambda}}{1.8}, \\ 0.4 & \text{for } a > \frac{\bar{\lambda}}{1.8} \end{cases} \quad (11)$$

We note that the RAT efficiency power index of -2.7 and the transition of $\bar{\lambda}/1.8$ differ slightly from the slope of -3 and $\bar{\lambda}/2.7$ in Hoang et al. (2021). However, this discrepancy in the torques is very small, as shown in their Figure 1.

2.3.2. Angular Velocity and Grain Alignment Size

RATs can spin up the irregular grain to a finite angular velocity (ω_{RAT}). The maximum angular velocity that an irregular grain is gained by RAT is given as

$$\omega_{\text{RAT}} = \frac{\bar{\Gamma}_{\text{RAT}} \tau_{\text{damp}}}{I_a} \quad (12)$$

where $I_a = 8\pi\rho a^5/15$ with ρ the grain mass density is the grain moment of inertia, and τ_{damp} is the rotational damping time which characterizes the damping caused by gas-grain collisions followed by evaporation and infrared emission.

The rotational damping timescale is given by

$$\tau_{\text{damp}} \simeq 8.3 \times 10^3 \left(\frac{a}{0.1 \mu\text{m}} \right) \left(\frac{\rho}{3 \text{ g cm}^{-3}} \right) \times \left(\frac{10^3 \text{ cm}^{-3}}{n_{\text{H}}} \right) \left(\frac{10 \text{ K}}{T_{\text{gas}}} \right)^{1/2} \left(\frac{1}{1 + F_{\text{IR}}} \right) \text{ yr} \quad (13)$$

where F_{IR} is the ratio of damping timescales between the gas collision and the infrared emission, which is approximately given by

$$F_{\text{IR}} = 0.038 \times U^{2/3} \left(\frac{0.1 \mu\text{m}}{a} \right) \left(\frac{10^3 \text{ cm}^{-3}}{n_{\text{H}}} \right) \left(\frac{10 \text{ K}}{T_{\text{gas}}} \right)^{1/2}. \quad (14)$$

One can observe that when $F_{\text{IR}} \ll 1$ (for instance, when $U^{2/3}/n_{\text{H}} \ll 1$), the damping timescale of the grain is influenced by the density and temperature of the gas. Conversely, if $F_{\text{IR}} \gg 1$ (for example, $U^{2/3}/n_{\text{H}} \gg 1$), the damping timescale $\tau_{\text{damp}} \sim n_{\text{H}}^{-1} T_{\text{gas}}^{-1/2} F_{\text{IR}}^{-1}$ becomes unaffected by the gas density and temperature. In starless cores, the former scenario is applicable.

The alignment of the grain remains effective if its angular velocity is three times higher than the thermal angular velocity ($(k_{\text{B}} T_{\text{gas}}/I_a)^{1/2}$) (see Hoang & Lazarian 2008). Therefore, the minimum grain size of grains that can be effectively aligned (referred to as the alignment size a_{align}) is the solution of the following equation:

$$\omega_{\text{RAT}}(a \equiv a_{\text{align}}) = 3 \times \left(\frac{15 k_{\text{B}} T_{\text{gas}}}{8\pi\rho a_{\text{align}}^5} \right)^{1/2}. \quad (15)$$

2.3.3. Alignment function

The alignment of grains with the ambient magnetic field can be characterised by two processes: internal alignment (where the grain's minor axis aligns with its angular momentum, J , see e.g. Spitzer & McGlynn 1979) and external alignment (where the angular momentum aligns with a preferred axis, which could be the ambient magnetic field, radiation field, gas flow; see Tram & Hoang 2022 for a review). The efficiency of internal alignment is described by Q_X , while it is Q_J for external alignment. The net grain alignment efficiency is quantified by the Rayleigh reduction factor of $R(a) = \langle Q_X Q_J \rangle$ where the brackets denote the average over an ensemble of grains of the given size a (see Hoang et al. 2015). Since grains aligned at high- J attractors have perfect internal alignment due to suprathermal rotation, i.e., $Q_X = 1$. One can approximately write $R \simeq f_{\text{high-J}}$.

The MRAT theory predicts the dependence of f_{high} with the local gas density and the grain magnetic properties, and $f_{\text{high-J}} = 1$ for superparamagnetic grains (Lazarian & Hoang 2008; Hoang & Lazarian 2016). Numerical calculations of grain alignment using the MRAT theory in Hoang & Lazarian (2016) show that the degree of alignment tends to increase smoothly with grain size, which was also obtained from inverse modelling of starlight polarisation (Hoang et al. 2014). Therefore, one can parameterise the alignment function as

$$f(a) = f_{\text{max}} \left[1 - e^{-(0.5a/a_{\text{align}})^3} \right], \quad (16)$$

which implies $f(a) = f_{\text{max}}$ for $a \gg a_{\text{align}}$ and $f(a) \rightarrow 0$ for $a \ll a_{\text{align}}$. The case of $f_{\text{max}} = 1$ is referred to as a perfect alignment of large grains by RATs.

2.4. Degree of Dust Polarisation

2.4.1. Starlight Polarisation

The degree of starlight polarisation for a population of dust, along a certain line of sight, is

$$p_{\text{ext}}(A_{\text{V}}) = 100 \times \int_s n_{\text{H}} ds \left(\int_{a_{\text{min}}}^{a_{\text{max}}} \frac{1}{2} \pi a^2 Q_{\text{ext}}^{\text{pol}} F_{\text{turb}} \sin^2 \psi f(a) \frac{1}{n_{\text{H}}} \frac{dn}{da} da \right) \% \quad (17)$$

where ψ is the inclination angle of the magnetic field orientation to the line of sight, F_{turb} is the turbulence factor, characterising the fluctuation of the magnetic field, $Q_{\text{ext}}^{\text{pol}}$ is the extinction polarisation coefficient. This efficiency is determined by the residual of the extinction efficiencies in the two components, where the electric field is parallel and perpendicular to the grain rotation axis (\mathbf{a}) as $0.5 [Q_{\text{ext}}(\mathbf{E} \parallel \mathbf{a}) - Q_{\text{ext}}(\mathbf{E} \perp \mathbf{a})]$. These components are taken from ASTRODUST database². Here, $F_{\text{turb}} = 0.5 [3 \langle \cos^2(\Delta\theta) \rangle - 1]$, where $\Delta\theta$ denotes the angular deviation between the local magnetic field and the average field (see Truong & Hoang 2024). As local and average fields are difficult to disentangle, F_{turb} is hard to define in general. However, when the cloud is sub-Alfvénic, that factor can be estimated via the angle dispersion of the magnetic fields $\delta\theta$ as $F_{\text{turb}} \simeq 1 - 1.5(\delta\theta)^2$. The expression $F_{\text{turb}} \times \sin^2 \psi$ in Equation 17 determines the influence of changes in magnetic fields, both in 3D orientations and fluctuations. For ease of understanding, we assume $F_{\text{turb}} = 1$ and $\psi = 90^\circ$ in subsequent sections, but discuss its effect in the Pipe-109 case study. A discussion of how field variation influences results can be found in Section 4.4.

² <http://arks.princeton.edu/ark:/88435/dsp01qb98mj541>

Table 1: Input parameters

Parameter	Value	Description
$n(\text{H}_2)$	$1.4 \times 10^5 \text{ cm}^{-3}$	Gas density at the core
α	-2	Slope of gas density
r_{flat}	0.04 pc	Radius of the core
r_{out}	0.6 pc	Outer radius of the cloud
U_0	3	External radiation field at the surface
γ	0.3	Anisotropic degree of ext. radiation field
$\bar{\lambda}_0$	$1.2 \mu\text{m}$	Mean-wavelength of ext. radiation field
$T_{\text{gas},0}$	16.4 K	Gas temperature at the surface
β	-3.5	Power index of grain size distribution
f_{max}	1.0	Maximum alignment efficiency
ψ	90°	Inclination angle of magnetic field
F_{turb}	1.0	Turbulence factor of magnetic field

Notes. For demonstration purposes, F_{turb} is assigned a value of 1.0, representing a uniform magnetic field. It is advised to determine the appropriate value tailored to each specific target. In this study, for Pipe-109, we compute F_{turb} as 0.98, 0.96, and 0.91 for the R-, H-bands, and submillimeter wavelengths respectively.

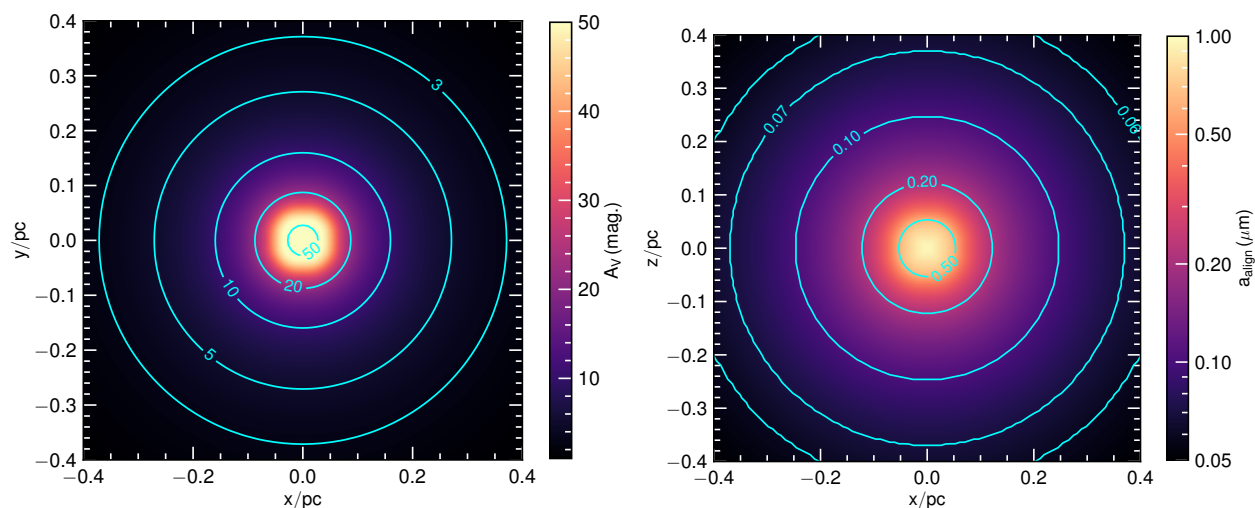


Fig. 2: **(Left)**: the full map on the plane of the sky ($\hat{x}\hat{y}$ plane) of the line of sight visual extinction. **(Right)**: the alignment size along the line of sight ($\hat{x}\hat{z}$ plane). We adopt $n_0 = 1.4 \times 10^5 \text{ cm}^{-3}$, $r_{\text{flat}} = 0.04 \text{ pc}$, $\alpha = 2$, $U_0 = 3$, $\gamma = 0.3$, the oblate grain (axial ratio of 1.4) with $a_{\text{max}} = 1 \mu\text{m}$, $\beta = -3.5$ and $f_{\text{max}} = 1$. This setup mimics the scale of the Pipe-109 starless core, whose data will be used later in this work.

2.4.2. Thermal Dust Polarisation

With a uniform magnetic field orientation, the total and polarised intensity can be estimated analytically, as described by Cho & Lazarian (2005); Lee et al. (2020); Tram et al. (2021a); Hoang & Truong (2024); Tram et al. (2024). The total emission intensity at a given position along a line of sight (denoted by r_i in Figure 1) is computed as

$$dI_{\text{em}} = n_{\text{H}} ds \times \int_{a_{\text{min}}}^{a_{\text{max}}} Q_{\text{abs}} \pi a^2 \times B_{\lambda}(T_{\text{d}}) \frac{1}{n_{\text{H}}} \frac{dn}{da} da. \quad (18)$$

Naturally, this intensity depends on the line of sight A_{V} , as determined in Equation 1. $B_{\lambda}(T_{\text{d}})$ is the black-body radiation at dust temperature T_{d} , Q_{abs} is the extinction coefficient and a function of a and λ . In this study, we assume that T_{d} and radiation intensity are in equilibrium and, consequently, we disregard the T_{d} distribution, which contrasts with the previous configuration in DUSTPOL-PY. This assumption is particularly justifiable for starless cores, where grains are probably large, making the nanodust

contribution insignificant. The distribution T_{d} for large grains is a delta function (see Figure 8 in Lee et al. 2020).

The local polarized intensity of thermal dust at the same location r_i as above is given by

$$dI_{\text{pol}} = n_{\text{H}} ds \times \int_{a_{\text{align}}}^{a_{\text{max}}} f(a) F_{\text{turb}} \sin^2 \psi Q_{\text{abs}}^{\text{pol}} \pi a^2 \times B_{\lambda}(T_{\text{d}}) \frac{1}{n_{\text{H}}} \frac{dn}{da} da, \quad (19)$$

where $Q_{\text{abs}}^{\text{pol}}$ is the absorption polarisation efficiency, determined by $0.5 [Q_{\text{abs}}(\mathbf{E} \parallel \mathbf{a}) - Q_{\text{abs}}(\mathbf{E} \perp \mathbf{a})]$. These components are also taken from the ASTRODUST database. As we can see, the angle ψ scales the amplitude of the degree of polarisation, but does not influence the shape of the spectrum, and the degree is maximum for $\psi = 90^\circ$ (i.e. the magnetic field is completely on the plane of the sky). In the following, we therefore consider the case of $\psi = 90^\circ$ and discuss its effect later.

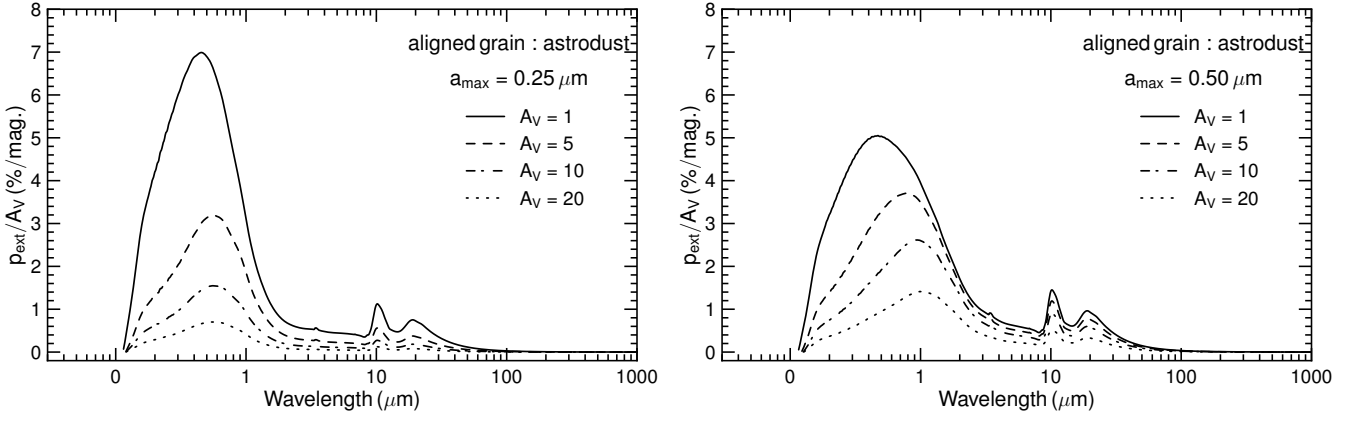


Fig. 3: The polarisation spectrum p_{ext}/A_V vs. λ of the starlight dust polarisation with different line of sight (A_V^{los}) for a maximum grain size of $0.25 \mu\text{m}$ (left panel) and of $0.5 \mu\text{m}$ (right panel). For $\lambda \leq 10 \mu\text{m}$, the spectrum feature is broader for larger maximum grain size. When A_V is low, smaller a_{max} yields a greater amplitude; however, this relationship inverts when A_V increases. The oblate grain with an axial ratio of 1.4 is adopted.

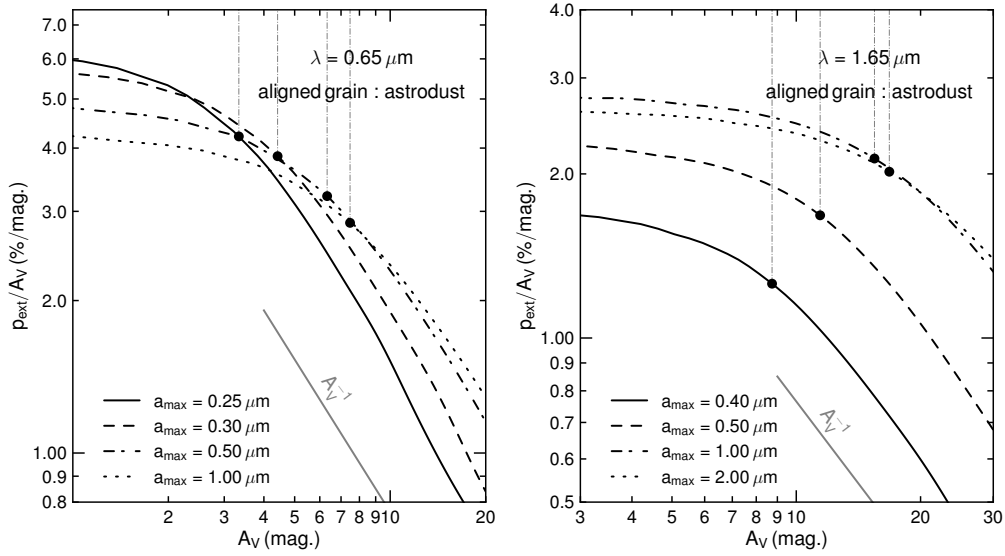


Fig. 4: The relation of p/A_V and A_V for the starlight polarisation at an optical wavelength (R-band, left panel) and at a near-IR wavelength (H-band, right panel). Different lines are for different maximum grain sizes. The dots and vertical lines are located where the slope changes from < -1 to -1 .

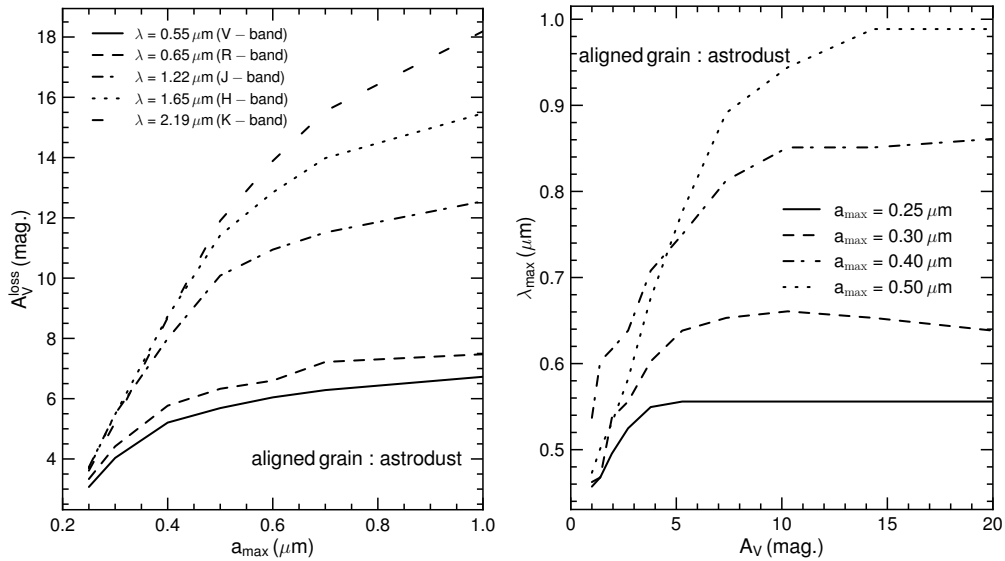


Fig. 5: **(Left)**: The relation of A_V^{loss} , where the grain loses completely its alignment, with the maximum grain size. This plot is made for several commonly used wavelengths for observations from the optical to the near-IR. **(Right)**: The relationship of the wavelength at the peak starlight polarisation (λ_{max}) with A_V . λ_{max} shows an increasing trend and remains steady with increasing A_V .

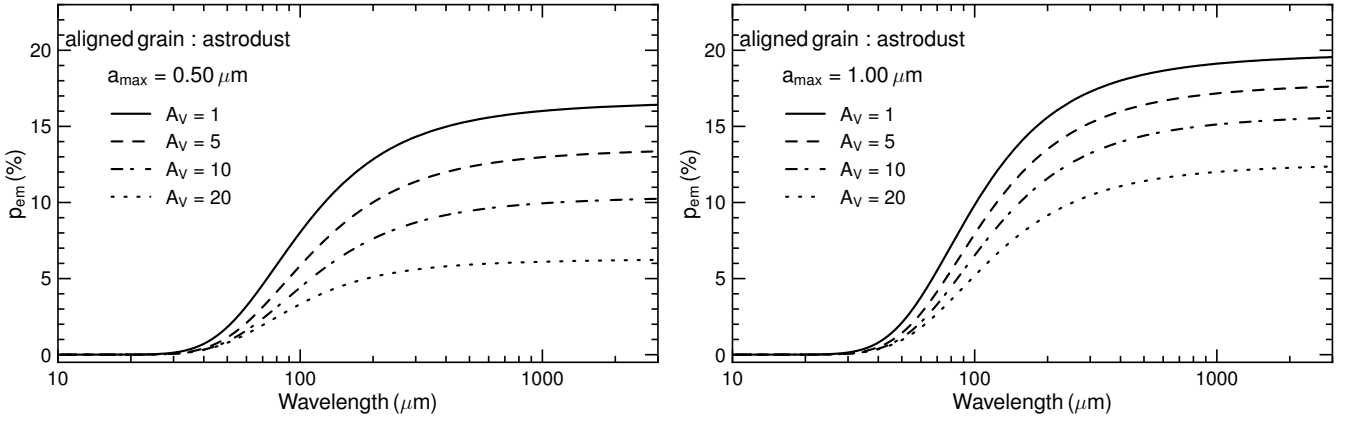


Fig. 6: The polarisation spectrum of thermal dust polarisation toward starless core with different values of the line-of-sight visual extinction (A_V^{los}), for $a_{\text{max}} = 0.5 \mu\text{m}$ (left panel) and $a_{\text{max}} = 1.0 \mu\text{m}$ (right). The spectrum first rapidly and then gradually increases towards longer wavelengths. Higher a_{max} yield higher degree of polarisation at the same physical condition (characterised by A_V).

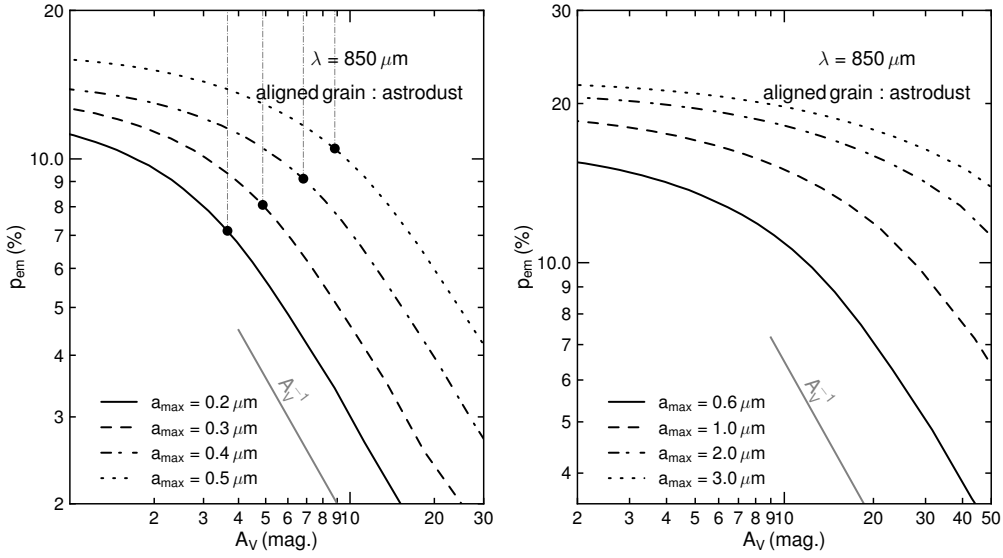


Fig. 7: The $p_{\text{em}} - A_V$ relation at $850 \mu\text{m}$ with different maximum grain sizes. The grey line shows the slope of -1 , which indicates a total loss of alignment in the grains. Smaller grains quickly lose their alignment within the cloud (left panel). If the grains are sufficiently large, the alignment is not completely lost (right panel). The black dots and the vertical dashed lines locate the value of A_V^{loss} .

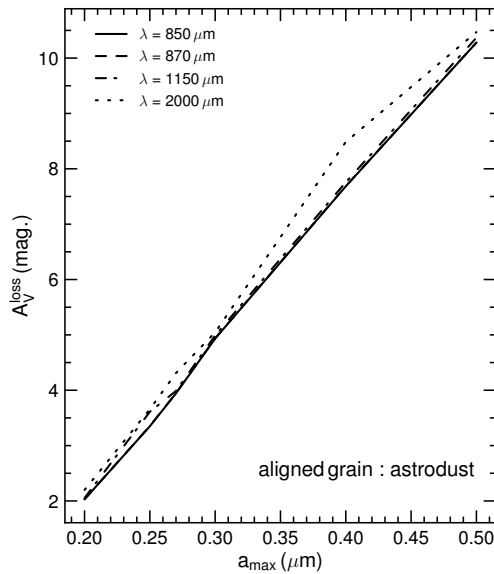


Fig. 8: The relations between A_V^{loss} and a_{max} at various submillimeter to millimeter wavelengths are analyzed for both current and upcoming instruments. Given our input parameters, grains larger than $0.5 \mu\text{m}$ maintain alignment across the cloud, leading to no A_V^{loss} beyond this size. At these wavelengths, the patterns remain consistent for these grain sizes.

The degree of thermal dust polarisation along a given line of sight is computed as

$$p_{\text{em}}(A_V) = 100 \times \frac{\int_s dI_{\text{pol}}}{\int_s dI_{\text{em}}} \quad (\%) \quad (20)$$

3. Numerical Results

3.1. Physical Properties

We aim to compare the polarisation degree from observations for starless cores, such as Pipe-109 with a maximum A_V at a centre of 50 mag. Thus, we particularly adopt $n(\text{H}_2) = 1.4 \times 10^5 \text{ cm}^{-3}$ at the centre, $r_{\text{flat}} = 0.04 \text{ pc}$ and $r_{\text{out}} = 0.6 \text{ pc}$ for our starless core setup (see Section 4.1), the density decreases towards the envelope as r^{-2} . The interstellar radiation field is taken as $U_0 = 3$ with $\gamma = 0.3$ (for a dense core; see Bethell et al. 2007). For grain alignment, we consider the perfect alignment of large grains of size $a \gg a_{\text{align}}$ with the magnetic field by the MRAT mechanism (Hoang & Lazarian 2016) and set $f_{\text{max}} = 1$. The summary of the parameters is given in Table 1.

We make the following key assumptions. Along an individual line of sight, while the physical profiles (gas density, temperature, radiation field, etc.) locally vary, we keep a_{max} as a constant along this line of sight, even though a_{max} would not be the same for each location on this line of sight.

The left panel of Figure 2 displays the map of visual extinction (A_V) in the V band ($0.55 \mu\text{m}$) along each line of sight in the plane of the sky ($\hat{x}\hat{y}$). As one moves towards the centre, the gas density sees a sharp increase, and the core's width becomes wider, leading to a higher A_V . The right panel of Figure 2 shows the alignment size map (a_{align}) in the plane of the line of sight ($\hat{x}\hat{z}$). From the periphery to the centre, not only does the gas density increase but also the radiation field notably decreases, while its mean wavelength is longer, resulting in a larger alignment size. Thus, to remain aligned deeper into the cloud, the average grain size must be larger.

3.2. Starlight polarisation (extinction polarisation)

Figure 3 shows the spectrum of starlight polarisation of p_{ext}/A_V (known as the polarisation efficiency) shown in Equation 17 for different A_V . The degree of polarisation is lower deeper inside the starless core (higher A_V). The polarisation features are strongest from the optical to mid-IR, and then dramatically drop to longer wavelengths. Compared to the smaller a_{max} , the larger grain size shows that the maximum value of p_{ext}/A_V is lower for low A_V but higher for higher A_V , and the degree of polarisation in the silicate absorption characteristic at $\lambda = 10, 18 \mu\text{m}$ is higher. Moreover, the spectrum is wider for larger a_{max} . These arise from the contribution of larger aligned grains.

Figure 4 illustrates the relationship between p_{ext}/A_V and the line of sight A_V at two specific wavelengths: an optical wavelength (R-band at $0.65 \mu\text{m}$, left panel) and a near-IR wavelength (H-band at $1.65 \mu\text{m}$, right panel). Generally, the polarisation efficiency decreases rapidly as A_V increases. At above a certain A_V^{loss} , $p_{\text{ext}}/A_V \sim A_V^{-1}$, which implies no polarisation signal when $A_V \geq A_V^{\text{loss}}$. The value of A_V^{loss} from the shallow to the steep slope is marked by black dots and vertical dashed lines³. The reason for this is straightforward: towards higher A_V , a_{align} becomes larger and the polarisation is not generated where $a_{\text{align}} > a_{\text{max}}$.

³ The values of A_V^{loss} is determined by a piecewise linear fitting using PWLF-library (Jekel & Venter 2019).

For a larger grain size that still maintains its alignment much deeper inside the cloud (higher A_V), the A_V^{loss} is higher compared to smaller sizes. Consequently, the polarisation in the optical band, at the surface, is higher for smaller grain sizes, as expected. In contrast, deeper inside the cloud, the alignment of the small grains is soon completely lost, while that of the larger grains remains.

A similar trend is observed for the H band shown in the right panel, but there are distinct characteristics that the alignment efficiency is lower for smaller a_{max} when the grain size is sufficiently small compared to the wavelength (that is, for $a \leq \lambda/1.8$, the radiative torque rapidly reduces for smaller grain size; see Equation 11). The left panel of Figure 5 shows the dependence of A_V^{loss} on a_{max} for several wavelengths in optical and near-IR (commonly used in observations). We can see that the value of A_V^{loss} is very sensitive to a_{max} . Longer wavelength observations are capable of detecting dust polarisation at greater depths within the cloud.

It can also be seen from Figure 3 that the wavelength λ_{max} (where the polarisation spectrum reaches its maximum in the UV-NIR range), is longer for higher A_V . The right panel of Figure 5 illustrates the relationship between λ_{max} and A_V . As A_V increases, λ_{max} initially increases and then becomes constant. The former increase is due to the increase in the gas density. The values of A_V above which λ_{max} is saturated are higher for larger a_{max} . Furthermore, one can see that λ_{max} is longer for larger a_{max} . These features arise because larger grains are capable of aligning more deeply within the cloud. The trend is seen to be similar to previous studies in Whittet et al. (2008); Hoang et al. (2015); Vaillancourt et al. (2020).

3.3. Polarisation Spectrum of Thermal Dust Polarisation

Figure 6 demonstrates the polarisation spectrum for the thermal dust emission from Equation 20 for different lines of sight. It initially exhibits an upward trend in the spectral profile, which then is constant at longer wavelengths. The spectra maintain their trend but vary in absolute values for different lines of sight A_V . The notable distinction is that larger grain sizes yield a greater degree of polarisation p_{em} compared to smaller sizes under the same physical conditions.

Figure 7 demonstrates the association between p_{em} and A_V at a wavelength of $850 \mu\text{m}$. This linkage, defined by the $p_{\text{em}} - A_V$ relation, signifies alignment efficiency similar to the $p_{\text{ext}}/A_V - A_V$ relation for starlight, primarily because the n_{H} term is cancelled out, though n_{H} indirectly influences alignment size. Typically, as one approaches the centre, the degree of polarisation decreases approximately following the relation $p_{\text{em}} \sim A_V^{-\eta}$. This slope is lower than 1 in the envelope and close to 1 in proximity to the core. The physical reason for this sudden drop is the loss in aligned grains (or a higher a_{align} shown in Figure 2). As expected, the locations in A_V^{loss} , above which the slope changes from $\eta < 1$ to ~ 1 , are observed to be higher for the larger grains a_{max} because these grains remain aligned much deeper within the core, shown by the black dots and vertical lines on the left panel. This can explain the well-known polarisation hole. Consequently, for larger grains ($a_{\text{max}} > a_{\text{align}}$), the slope η is much shallower than 1, resulting in no polarisation hole (right panel). It should be noted that this critical intensity transition is mainly dependent on the maximum grain size (a_{max}) and independent of the grain composition and the maximum alignment factor f_{max} . It is interesting to note that the slope can be slightly higher than 1 in case of no

alignment because of the integration with different gas densities along the line of sight.

Figure 8 illustrates the correlation between A_V^{loss} and a_{max} for values up to $0.5 \mu\text{m}$ (for the input parameters used in this work), relevant to submillimetre and millimetre wavelengths, such as those utilised by JCMT/POL-2 at $850 \mu\text{m}$, and that will be used by APEX/A-MKID at $870 \mu\text{m}$ and IRAM/NIKA-2 at 1.15 and 2 mm. The relationship remains consistent at these wavelengths. For higher a_{max} , A_V^{loss} cannot be determined, as shown in the right panel of Figure 7, because larger grain sizes can be aligned across the cloud.

4. Discussions

4.1. Application to Pipe-109 Starless Core

We now compare our modelling results with observational data from a specific starless core Pipe-109 (another name FeSt 1-457). Firstly, we adjust the parameters r_{flat} and r_{out} accordingly to this specific target. To do so, we compare the line-of-sight visual extinction predicted by our model to the one observed as shown in Figure 1 of Alves et al. (2014) with $A_V = 50$ mag in the centre. The map A_V on the left panel of the sky plane in Figure 2 (for $\alpha = 2$ and $a_{\text{max}} = 1 \mu\text{m}$) matches closely to the one of the Pipe-109, corresponding to $r_{\text{flat}} = 0.04$ pc and $r_{\text{out}} = 0.6$ pc.

Then, the comparisons of the p_{ext}/A_V and p_{em} versus A_V between our model predictions with a fixed grain elongation (oblate grain with an axial ratio of 1.4) and observations are illustrated in Figure 9 for the specific case of the Pipe-109 starless core, whose data are adopted from Alves et al. (2014). This comparison consistently considers three different wavelengths: $0.65 \mu\text{m}$ (optical, first row) and $1.65 \mu\text{m}$ (near-IR, second row), and $850 \mu\text{m}$ (submillimeter, third row). From the model, we only vary the maximum grain size a_{max} , shown by different lines. One can see that in order to reproduce the data, a_{max} must be higher for dust polarisation at longer wavelengths. In detail, using the parameters sets mentioned above, our model predicts that the maximum grain size ranges from $0.19 \leq a_{\text{max}} \leq 0.25 \mu\text{m}$ at a wavelength of $0.65 \mu\text{m}$, from $0.25 \leq a_{\text{max}} \leq 0.35 \mu\text{m}$ at $1.65 \mu\text{m}$, and falls within $1 \leq a_{\text{max}} < 3 \mu\text{m}$ at $850 \mu\text{m}$. For visualisation, the combination of all wavelengths is shown in the fourth panel with the shaded areas corresponding to the best ranges of a_{max} . Note that the explicit values of a_{max} are subject to change with different sets of parameters, but the requirement for larger a_{max} at higher A_V is unchanged.

In particular, the presence of two separate slopes at $1.65 \mu\text{m}$, one is shallower for $A_V \gtrsim 14$ mag, appears evident, which a single model cannot replicate; however, distinct models with different values of a_{max} could match this trend, in which the shallower slope corresponds to a higher a_{max} . In general, there is a clear trend in increasing grain size towards the centre. Our finding might be consistent with the speculation in Alves et al. (2014), for which the optical and near-IR wavelengths originate from the envelope of the starless core, while the submillimeter observations originate from the core. However, even for $a_{\text{max}} = 3 \mu\text{m}$, our model cannot yet cover all data points at $850 \mu\text{m}$.

Figure 10 shows the comparison in which we fixed the values of $a_{\text{max}} = 0.19, 0.25$ and $1.0 \mu\text{m}$ for the R, H and submm bands (the lowest values of the range in Figure 9) and varied the grain axial ratio. In this case, the models cover the data better at $850 \mu\text{m}$, but the goodness of the comparison is less at near-IR with $A_V > 14$ mag. Considering both the influence of the maximum grain size and elongation, it becomes clear that to bet-

ter reproduce observations, one needs larger and more elongated grains deeper inside this starless core.

Figure 11 shows the comparison in the $p_{\text{em}} - I$ relation at $850 \mu\text{m}$ with a fixed grain axial ratio of 1.4 (top panel) and a fixed maximum grain size of $1 \mu\text{m}$ (bottom panel). The model can nicely reproduce the observational data for the same range of a_{max} and axial ratios shown in Figures 9 and 10. Furthermore, this figure attempts to compare directly with Figure 3 from Alves et al. (2014), where the authors used the DUSTPOL model in Padovani et al. (2012) and manually applied a fixed polarisation efficiency, adjusting it to 0.18 for gas densities up to $6 \times 10^4 \text{ cm}^{-3}$ and setting it to zero beyond that range. Specifically, the DUSTPOL model referenced in Padovani et al. (2012) does not account for the physics of alignment; instead, it treats alignment as an adjustable parameter (α). Thus, our new physical modelling based on RAT physics provides a better approach to understanding the dust polarisation in starless cores.

4.2. Implication for grain alignment: magnetically enhanced radiative torque (MRAT)

The successful fitting of the multiwavelength polarisation data observed toward the starless core Pipe-109 with the RAT alignment model with the maximum alignment degree of $f_{\text{max}} = 1$ and the composite ASTRODUST model suggests the perfect alignment of large magnetic dust grains of $a \gg a_{\text{align}}$. To achieve such a perfect alignment, the classical RAT theory alone is insufficient, necessitating MRAT (Lazarian & Hoang 2008; Hoang & Lazarian 2016). This is the first evidence of the MRAT in starless cores. However, previously, the MRAT evidence was supported by various studies for the diffuse ISM (Hensley & Draine 2023) and molecular clouds (Reissl et al. 2020). Recently, dedicated models with proper treatments for the internal and external alignment processes in Giang et al. (2023); Giang & Hoang (2024); Thang et al. (2024); Giang et al. (2024) showed that MRAT with iron inclusions is required to understand the dust polarisations in protostars, low- and intermediate-mass young stellar objects and protoplanetary disk by ALMA.

We note that a lower value of f_{max} can be allowed (and no need for the MRAT, i.e., classical RAT theory is sufficient) if the grain elongation is increased to have the axial ratio greater than 3 or the radiation intensity is more intense that compensates for the strong randomisation of grain alignment by dense gas collisions. The first case may be possible because we showed that grain growth (increase in a_{max}) is accompanied by an increase in the grain elongation, but such extremely elongated grains would not survive the various destruction mechanisms such as shattering or disruption (see Draine 2024). The second case results in a higher degree of polarisation deeper within the cloud, making p vs. A_V shallower. However, there is no evidence of a nearby strong radiation source for the Pipe-109 core.

4.3. How do grains grow in starless cores?

Grain growth is expected to occur in dense clouds due to gas accretion and grain-grain collisions (see, e.g., Hirashita & Li 2013), but the detailed physics of grain growth is not well understood. Traditionally, grain growth is usually assumed to be isotropic because of the random motion of gas and grains, which results only in the increase in the grain size. However, a recent study by Hoang (2022) showed that, due to grain alignment with ambient magnetic fields, grain growth becomes anisotropic. As a

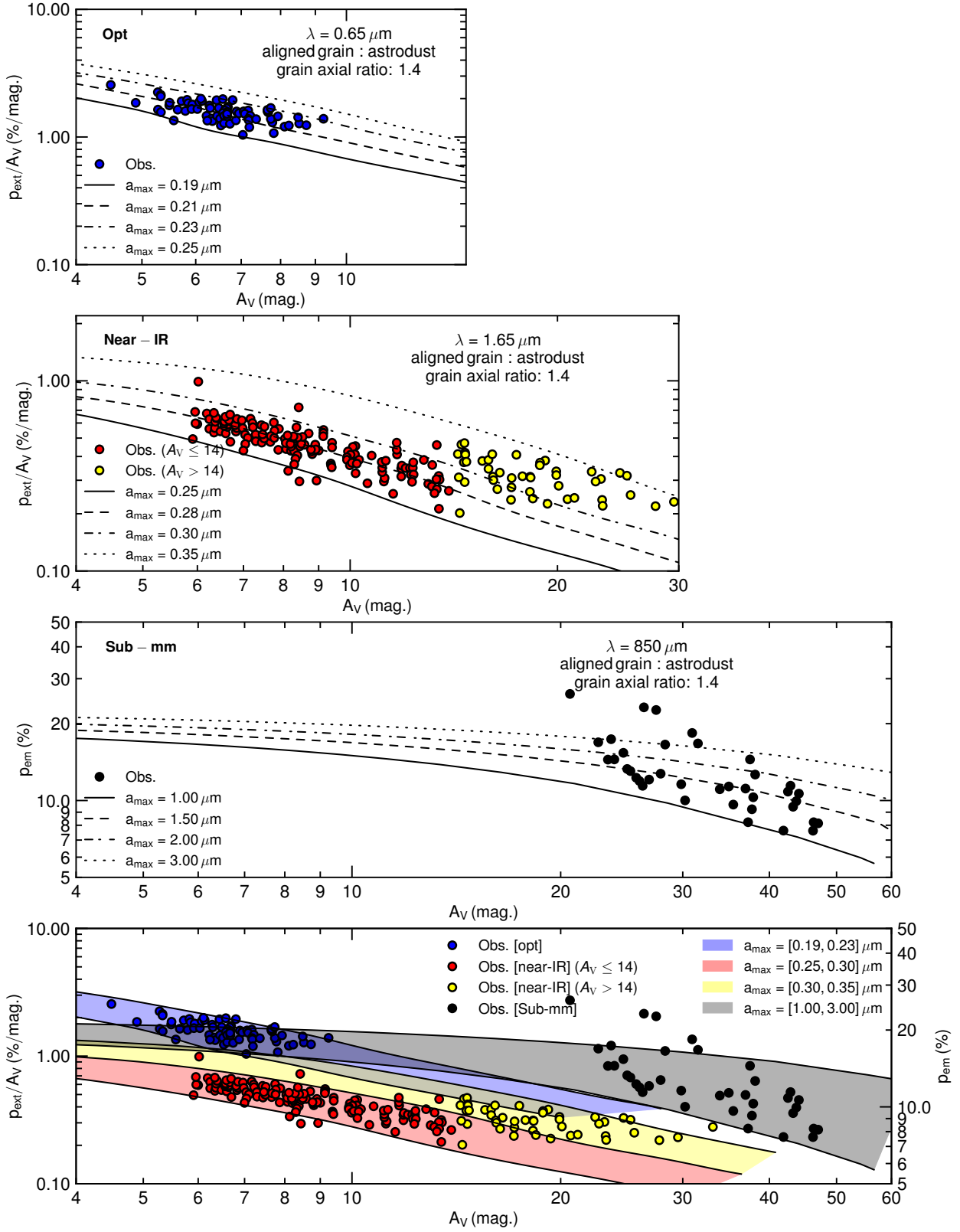


Fig. 9: The comparison of our model’s predictions with grain axial ratio of 1.4 as a function of A_V from the surface to the core and actual observations directed towards the Pipe-109 starless core is presented here. In the optical range (first row) and near-IR range (second row), we plot p_{ext}/A_V (alignment efficiency) against A_V , while for submm data (third row), we use p_{em} versus A_V . The fourth row groups all the above datasets, with a shaded region indicating the range of a_{max} that nicely covers the data as shown in the above panels. Notably, longer wavelength polarisation is detected deeper inside the starless core (i.e., higher A_V). In order to match with the observations, the maximum grain size a_{max} must be greater as A_V increases. The models could not cover all data points at $850\ \mu\text{m}$ even at $a_{\text{max}} = 3\ \mu\text{m}$. Polarisation data is adapted from [Alves et al. \(2014\)](#) and references therein.

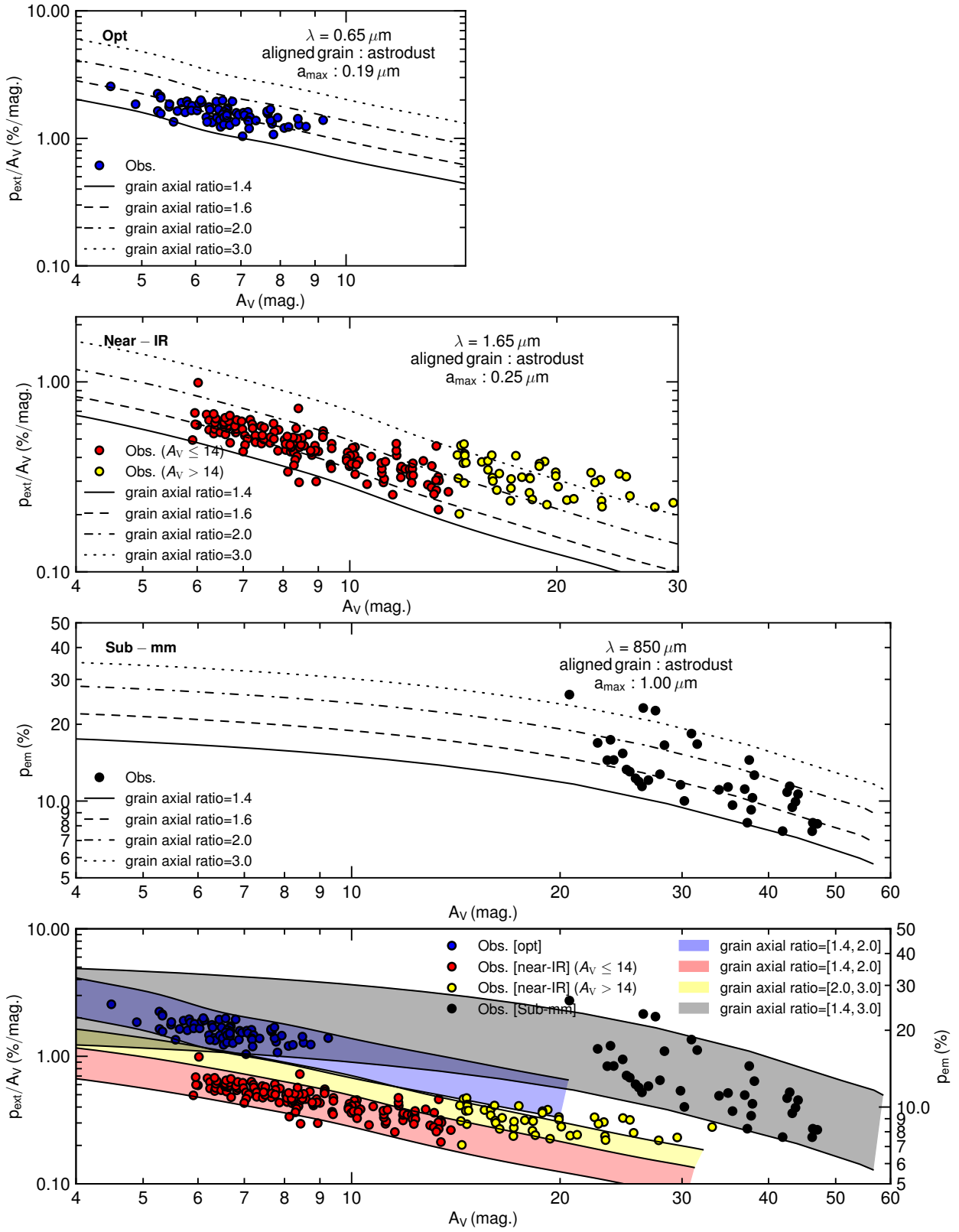


Fig. 10: Similar structure to Figure 9, but representing different grain elongations (axial ratio is varied) while keeping the maximum grain size constant, which respectively are 0.19, 0.25 and 1.0 μm (the lowest values in the a_{max} range shown in Figure 9). Models incorporating increased grain elongation match more closely with observations at 850 μm . However, for near-IR data with $A_V > 14$ mag, even at an axial ratio of 3, the model fails to cover all data, indicating the need for the existence of larger grains, as shown in Figure 9. For optical and near-IR data with $A_V \leq 14$ mag, models are able to fit.

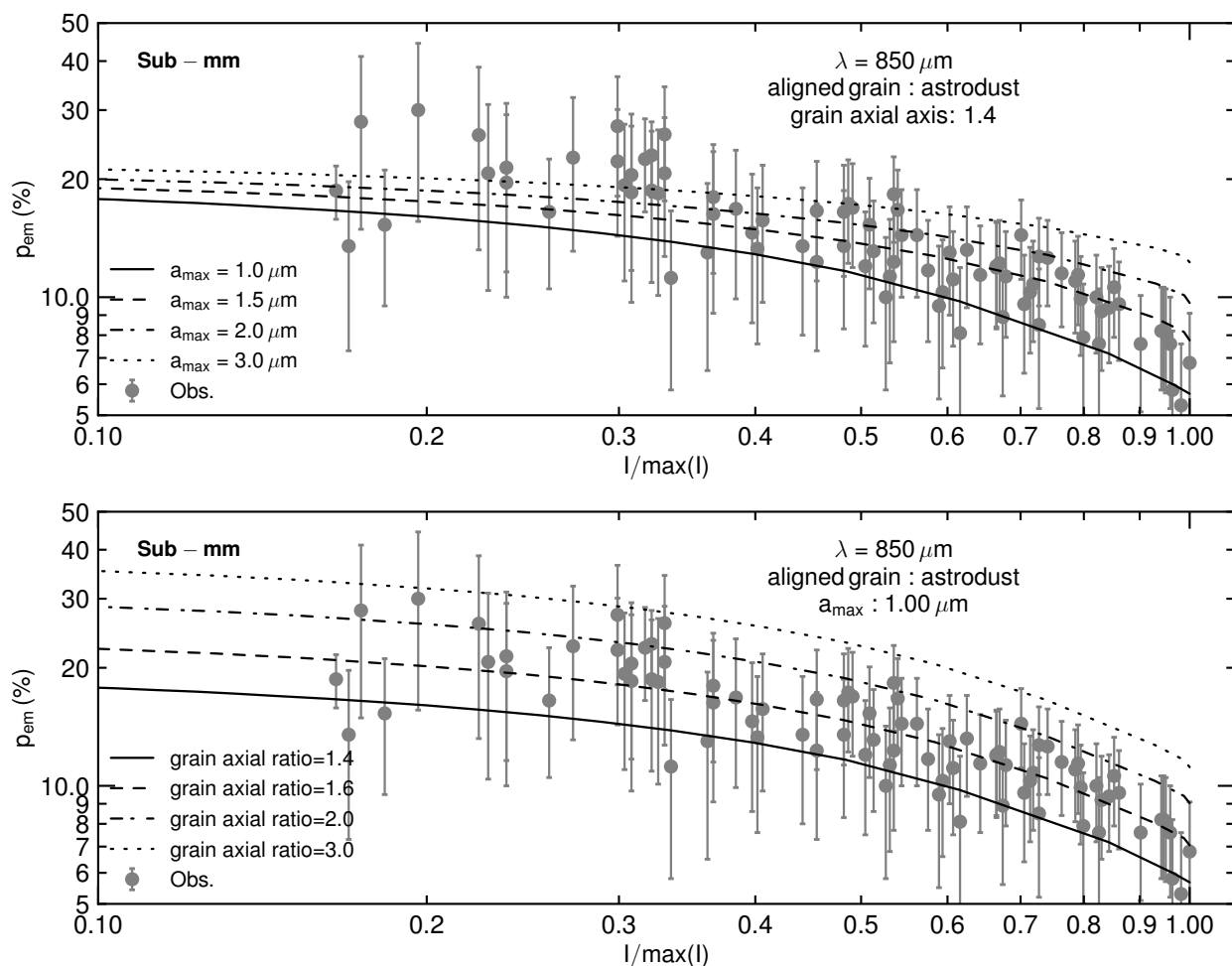


Fig. 11: Similar to Figures 9 and 10, but $p_{\text{em}} - I$ relationships for thermal dust polarization at $850 \mu\text{m}$. The top panel depicts a constant grain axial ratio with changes in the maximal grain size, whereas the bottom panel displays a variable grain axial ratio with a constant maximum grain size. The combination of large and elongated grains is required to reproduce these observations. Data is taken from the public data file in Alves et al. (2014).

result, the grain growth process can increase both grain size and elongation, and larger grains have higher elongation.

In the previous Section, we showed that the combination of starlight and thermal dust polarisation in starless cores clearly demonstrates the need for larger grains in a starless core, which implies significant grain growth in such dense environments. To examine the extent of grain growth in different environments, sufficient observations of various starless cores, each with distinct physical characteristics, are needed, because the reduction in the degree of polarisation with total intensity or visual extinction is different for varying a_{max} . Our proposed diagnosis for grain growth using the relation p_{ext}/A_V versus A_V shown in Section 3 differs from and complements the one previously described in Vaillancourt et al. (2020), in which the authors implied grain growth using the relation of the maximum wavelength λ_{max} with A_V from multiwavelength observations in optical to near-IR (see their Figure 5 or our Figure 5, right panel).

In particular, as shown in Figure 10, the higher the elongation at the larger A_V can reproduce the data successfully. For the maximum size of $a_{\text{max}} \leq 0.25 \mu\text{m}$, the grain elongation between 1.2 – 2 can reproduce the starlight polarisation data for $A_V < 14$, but it requires elongation of $\sim [2 - 3]$ to reproduce the data at $A_V \sim 10 - 30$. At $A_V > 30$, the high elongation of ~ 3 is required to reproduce the upper bound of the thermal dust polar-

isation data. This shows the first evidence for grain growth accompanied by an increase in grain elongation as predicted from the anisotropic grain growth model in Hoang (2022). Another possible mechanism that can make the grains more elongated is through the effect of the centrifugal force, which arises from the fast rotation of the grains by radiative torques (Reissl et al. 2024). However, in starless cores, the radiation field is rather weak and cannot efficiently make grains more elongated deeper inside the cores.

4.4. Effects of Magnetic Field Geometry

Our numerical modelling above assumed a uniform magnetic field in the plane of the sky. However, in realistic situations, the magnetic field varies along the LOS.

First, magnetic turbulence can cause fluctuations of the local magnetic field with respect to the mean magnetic field. Due to this effect, the degree of polarisation is lower by a factor of $F_{\text{turb}} < 1$ (see Equations 17 and 19). Using the polarisation angles outlined in Alves et al. (2014) for the Pipe-109 core, and assuming that this cloud is sub-Alfvénic, we compute turbulence factors F_{turb} of 0.98, 0.96, and 0.91 for optical, near-infrared, and submillimeter wavelengths, respectively. Evidently, the di-

vergence from a uniform magnetic field scenario is minor at 2%, 4%, and 9%, indicating that the influence of F_{turb} is insignificant for this specific instance of Pipe-109.

Second, the mean magnetic field may not lie in the position of the sky, instead making an angle ψ with respect to the POS. Numerical simulations for the formation of cores by Mocz et al. (2017) show that the inclination angle of the magnetic field varies from the outer to the inner region for the case of moderate and strong magnetic fields. Therefore, one cannot expect the magnetic field to be uniform, i.e., the same angle ψ from starless cores. In this case, the degree of polarisation will be reduced by a factor of $f_{\text{max}} \sin^2 \psi$ (see Equations 17 and 19). For Pipe-109, Kandori et al. (2018) studied magnetic fields using the NIR data and submm polarisation and found that the magnetic field can be described by a parabolic form. Kandori et al. (2020) applied the flux-freezing model from Myers et al. (2018) to this core and found that the best-fit model yields the inclination angle of $\psi = 35 \pm 15^\circ$. Therefore, the model with a fixed grain elongation of 1.4 could not reproduce the observational data with a_{max} mentioned above because the maximum polarisation degree is reduced by a factor of $\sin^2 35^\circ \approx 1/3$ compared to the ideal model of $\psi = 90^\circ$. This suggests that the elongation of grains must be enhanced to reproduce the observed polarisation.

To illustrate the effect of grain elongation on polarisation, in Figure 12, we show the polarisation spectrum of both starlight and thermal dust for oblate grains with axial ratios of 1.4 and 3. It is evident that more elongated grains result in higher polarisation. At the wavelengths discussed in this work (0.65, 1.65 and $850 \mu\text{m}$), the degree of polarisation for the axial ratio of 3 is at least twice that for the axial ratio of 1.4. Therefore, an accurate method to constrain the angle of inclination of the magnetic field would help constrain the grain elongation and grain growth physics (Hoang 2022).

4.5. p_{ext} vs. A_V and p_{ext} vs. I relations

Figure 13 shows the comparison between the $p_{\text{em}}-A_V$ and $p_{\text{em}}-I$ relations. One can see that the relation p_{em} versus I fundamentally shows similar patterns to p_{em} vs. A_V , but the slope is slightly different. The only reason we observed this difference is that the sight line A_V is not linearly correlated with the total intensity I , simply because $I_v \propto B_v(T_d)A_V$ and T_d is not a constant along the line of sight. In addition, it should be noted that for sufficiently large grains (i.e. $a_{\text{max}} \geq 0.6 \mu\text{m}$ for our input parameters), the relationship $p-A_V$ exhibits a slope less steep than -1 , as expected because $a_{\text{max}} > a_{\text{align}}$, while the relationship $p-I$, for the same a_{max} , characterises the polarisation hole with a slope I^{-1} . We therefore suggest that the $p-A_V$ relation is the proper diagnostic for observations.

4.6. Uncertainties

The most obvious sources of uncertainty in this work are the assumption that the maximum grain size remains unchanged along the line of sight and that we do not include any treatment of the grain evolution within the cloud. Proper models that consistently constrain the maximum grain size as a function of the physical condition could compare better with observations. However, as mentioned above, the quantitative value presented in this work might change, but the phenomena are expected not to be different. The assumption of being optically thin for emission of thermal dust satisfies at $850 \mu\text{m}$, but might cause uncertainty at shorter wavelengths (e.g. mid-IR to far-IR).

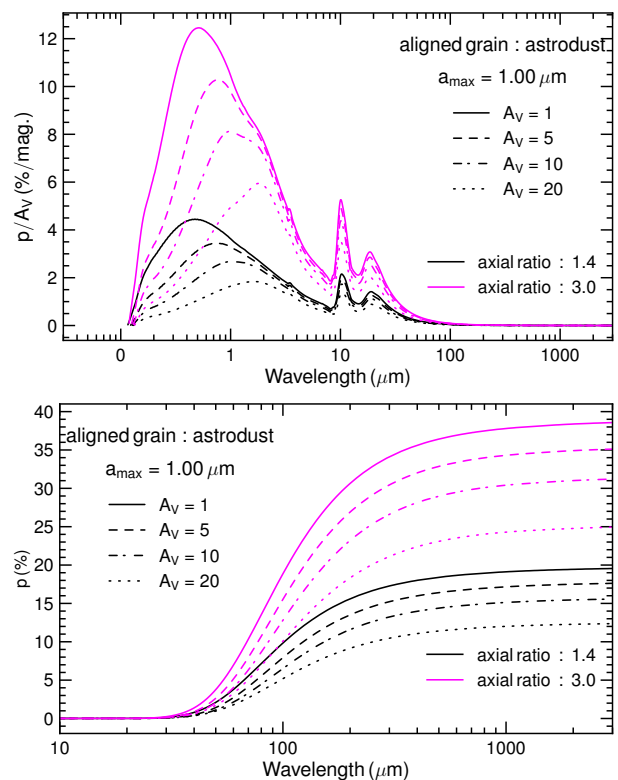


Fig. 12: The polarisation spectrum in absorption (top panel) and emission (bottom panel) for a maximum grain size $a_{\text{max}} = 1 \mu\text{m}$ with different axial ratios (1.4 and 3). The more elongated the grain, the higher the degree of polarisation.

We would like to note that, as long as the dust temperature varies along the line of sight, the visual extinction is not linearly correlated to the total intensity, making the p_{em} vs. I relation less accurate for analysing observations in externally heated cores. Finally, the proper integration of grain growth processes has not been incorporated, which serves as a major source of uncertainty.

5. Conclusions

Significant advances have been made in our understanding of dust grain alignment physics, alongside a substantial increase in high-quality multi-wavelength dust polarisation data. Grain growth in dense clouds is the first step in planetesimal formation. However, the detailed mechanisms of grain alignment, as well as the process of grain growth and its underlying physics, are not well understood. Starless cores, which exhibit minimal internal dynamics and have the potential to form young stars, serve as the simplest and most suitable targets to better understand these physical processes. In this study, we aim to constrain the physics of grain alignment by radiative torques and dust evolution using the multiwavelength dust polarisation observed toward starless cores. The main findings of our study are summarized as follows:

- We model multi-wavelength polarisation for both extinction (starlight) and emission polarisations using a new proposed composition of interstellar dust (ASTRODUST) and the MRAT alignment theory with perfect alignment of large grains for a starless core in which grains are aligned by attenuated interstellar radiation field. Different maximum grain sizes

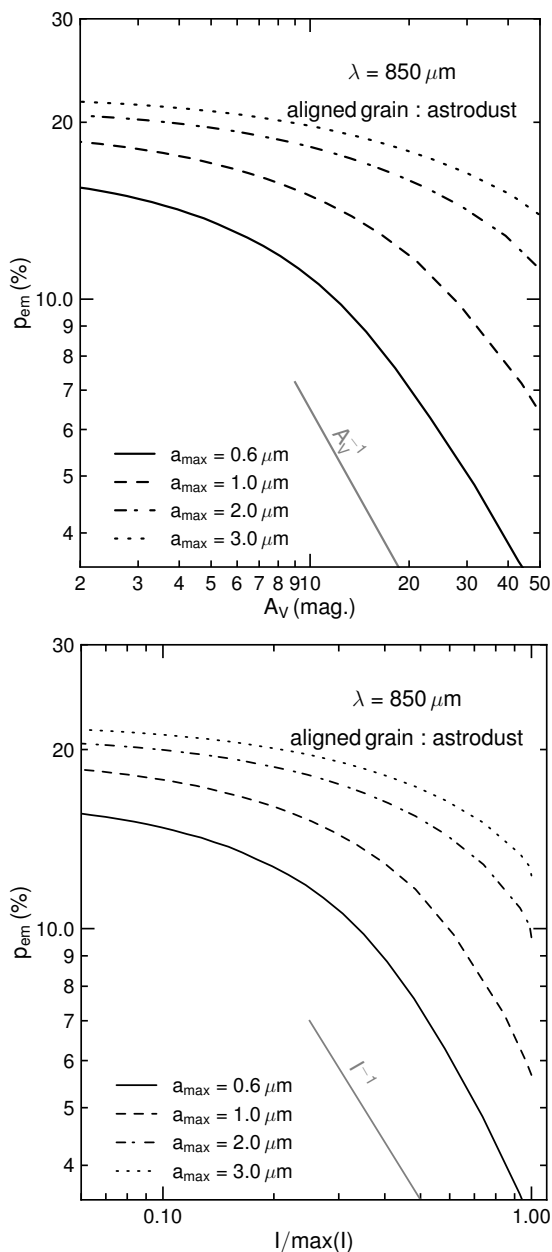


Fig. 13: Comparison between the p_{em} vs. A_V (from Figure 7, top right) and p_{em} vs I at submillimeter wavelength. For the same a_{max} , towards higher A_V , p_{em} drop with a slope shallower than 1, while the $p_{em} - I$ slope is shallower and even close to 1.

and elongations are considered, and the magnetic field is assumed to lie in the plane of the sky.

- Our model indicates that the reduction in the degree of polarisation towards the centre (referred to as the polarisation hole) is primarily caused by the loss of dust grain alignment of small grains in dense gas (due to gas collisional damping) and the decrease in radiation intensity (attenuation). Larger grains can still maintain alignment further into the core due to the effect of longer wavelength photons.
- We tailor our model to a particular case of the Pipe-109 core as a showcase. The results of our optimal polarization model (i.e., B-fields in the POS) can nicely reproduce the observational data consistently for optical (R band), near-IR (H band) and submillimeter ($850 \mu\text{m}$).

- In particular, we found that grains must be larger in size and more elongated in shape at higher visual extinction (deeper inside the cloud) to match observations. This is the first evidence for grain growth that involves both the maximum size and grain elongation, which is consistent with the anisotropic grain growth model for aligned grains.
- When considering the magnetic field’s inclination relative to the line of sight, the polarisation degree is noticeably reduced and can deviate significantly from observations. Therefore, the grain elongation must be significantly enhanced beyond $s \sim 3$, for which extreme elongated grains may not survive destruction processes.
- Finally, our model provides a promising tool for constraining the physics of grain alignment and grain evolution (GRADE-POL) using multi-wavelength dust polarisations.

Acknowledgements. The authors thank Dr. Isabelle Ristorcelli for the useful comments from the early phase of this work. T.H. acknowledges the support from the main research project (No. 2025186902) from Korea Astronomy and Space Science (KASI). This work was partly supported by a grant from the Simons Foundation to IFIRSE, ICISE (916424, N.H.). We thank the ICISE staff for excellent support and hospitality.

References

- Abbas, M. M., Craven, P. D., Spann, J. F., et al. 2004, *ApJ*, 614, 781
- Ahn, J., Xu, Z., Bang, J., et al. 2018, *Phys. Rev. Lett.*, 121, 033603
- Aitken, D. K., Smith, C. H., & Roche, P. F. 1989, *MNRAS*, 236, 919
- Alves, F. O., Frau, P., Girart, J. M., et al. 2014, *A&A*, 569, L1
- Andersson, B. G., Lazarian, A., & Vaillancourt, J. E. 2015, *ARAA*, 53, 501
- Andersson, B. G., Pintado, O., Potter, S. B., Straizys, V., & Charcos-Llorens, M. 2011, *A&A*, 534, A19
- Andersson, B. G. & Potter, S. B. 2010, *ApJ*, 720, 1045
- Bethell, T. J., Chepurnov, A., Lazarian, A., & Kim, J. 2007, *ApJ*, 663, 1055
- Bianchi, S. 2024, *Astronomy & Astrophysics*, 691, A330
- Borlaff, A. S., Lopez-Rodriguez, E., Beck, R., et al. 2023, *ApJ*, 952, 4
- Cho, J. & Lazarian, A. 2005, *ApJ*, 631, 361
- Cudlip, W., Furniss, I., King, K. J., & Jennings, R. E. 1982, *MNRAS*, 200, 1169
- Dolginov, A. Z. & Mitrofanov, I. G. 1976, *Ap&SS*, 43, 291
- Draine, B. 2024, *The Astrophysical Journal*, 961, 103
- Draine, B. T. 2011, *Physics of the Interstellar and Intergalactic Medium*
- Draine, B. T. & Hensley, B. S. 2021, *ApJ*, 909, 94
- Draine, B. T. & Weingartner, J. C. 1996, *ApJ*, 470, 551
- Geach, J. E., Lopez-Rodriguez, E., Doherty, M. J., et al. 2023, *Nature*, 621, 483
- Gerakines, P. A., Whittet, D. C. B., & Lazarian, A. 1995, *ApJ*, 455, L171
- Giang, N. C. & Hoang, T. 2024, *MNRAS*, 530, 984
- Giang, N. C., Hoang, T., Kim, J.-G., & Tram, L. N. 2023, *MNRAS*, 520, 3788
- Giang, N. C., Le Gouellec, V. J. M., Hoang, T., Maury, A. J., & Hennebelle, P. 2024, arXiv e-prints, arXiv:2407.10079
- Gupta, S., Soam, A., Karoly, J., Lee, C. W., et al. 2024, arXiv preprint arXiv:2412.19701
- Hall, J. S. 1949, *Science*, 109, 166
- Hensley, B. S. & Draine, B. T. 2023, *The Astrophysical Journal*, 948, 55
- Hensley, B. S. & Draine, B. T. 2023, *ApJ*, 948, 55
- Herranen, J., Lazarian, A., & Hoang, T. 2019, *ApJ*, 878, 96
- Herranen, J., Lazarian, A., & Hoang, T. 2021, *ApJ*, 913, 63
- Hiltner, W. A. 1949, *Science*, 109, 165
- Hirashita, H. & Li, Z.-Y. 2013, *MNRAS*, 434, L70
- Hoang, T. 2022, *ApJ*, 928, 102
- Hoang, T. & Lazarian, A. 2008, *MNRAS*, 388, 117
- Hoang, T. & Lazarian, A. 2016, *ApJ*, 831, 159
- Hoang, T., Lazarian, A., & Andersson, B. G. 2015, *MNRAS*, 448, 1178
- Hoang, T., Lazarian, A., & Martin, P. G. 2014, *The Astrophysical Journal*, 790, 6
- Hoang, T. & Tram, L. N. 2020, *ApJ*, 891, 38
- Hoang, T., Tram, L. N., Lee, H., & Ahn, S.-H. 2019, *Nature Astronomy*, 3, 766
- Hoang, T., Tram, L. N., Lee, H., Diep, P. N., & Ngoc, N. B. 2021, *ApJ*, 908, 218
- Hoang, T., Tram, L. N., Minh Phan, V. H., et al. 2022, *The Astronomical Journal*, 164, 248
- Hoang, T. & Truong, B. 2024, *The Astrophysical Journal*, 965, 183
- Holgate, J. T., Simons, L., Andrew, Y., & Stavrou, C. K. 2019, *EPL (Europhysics Letters)*, 127, 45004
- Hull, C. L. H., Plambeck, R. L., Kwon, W., et al. 2014, *ApJs*, 213, 13

- Jekel, C. F. & Venter, G. 2019, *pwlif*: A Python Library for Fitting 1D Continuous Piecewise Linear Functions
- Jones, T. J., Bagley, M., Krejny, M., Andersson, B. G., & Bastien, P. 2015, *AJ*, 149, 31
- Kandori, R., Nagata, T., Tazaki, R., et al. 2018, *The Astrophysical Journal*, 868, 94
- Kandori, R., Tomisaka, K., Saito, M., et al. 2020, *The Astrophysical Journal*, 888, 120
- Lazarian, A. & Hoang, T. 2007, *MNRAS*, 378, 910
- Lazarian, A. & Hoang, T. 2008, *ApJ*, 676, L25
- Lazarian, A. & Hoang, T. 2021, *ApJ*, 908, 12
- Lee, H., Hoang, T., Le, N., & Cho, J. 2020, *ApJ*, 896, 44
- Mathis, J. S., Mezger, P. G., & Panagia, N. 1983, *A&A*, 500, 259
- Mathis, J. S. & Whiffen, G. 1989, *ApJ*, 341, 808
- Mocz, P., Burkhart, B., Hernquist, L., McKee, C. F., & Springel, V. 2017, *The Astrophysical Journal*, 838, 40
- Myers, P. C., Basu, S., & Auddy, S. 2018, *The Astrophysical Journal*, 868, 51
- Ngoc, N. B., Hoang, T., Diep, P. N., & Tram, L. N. 2024, *arXiv e-prints*, arXiv:2403.16857
- Padovani, M., Brinch, C., Girart, J. M., et al. 2012, *A&A*, 543, A16
- Pattle, K., Fissel, L., Tahani, M., Liu, T., & Ntormousi, E. 2023, in *Astronomical Society of the Pacific Conference Series*, Vol. 534, *Astronomical Society of the Pacific Conference Series*, ed. S. Inutsuka, Y. Aikawa, T. Muto, K. Tomida, & M. Tamura, 193
- Planck Collaboration, Akrami, Y., Ashdown, M., et al. 2020, *A&A*, 641, A4
- Reimann, R., Doderer, M., Hebestreit, E., et al. 2018, *Phys. Rev. Lett.*, 121, 033602
- Reissl, S., Guillet, V., Brauer, R., et al. 2020, *Astronomy & Astrophysics*, 640, A118
- Reissl, S., Nguyen, P., Jordan, L. M., & Klessen, R. S. 2023, *arXiv:2301.12889*
- Reissl, S., Nguyen, P., Jordan, M. L., & Klessen, S. R. 2024, *Astronomy & Astrophysics*
- Spitzer, L., J. & McGlynn, T. A. 1979, *ApJ*, 231, 417
- Thang, N. T., Diep, P. N., Hoang, T., et al. 2024, *ApJ*, 970, 114
- Tielens, A. 1989, in *IAU Symposium*, Vol. 135, *Interstellar Dust*, ed. L. J. Allamandola & A. G. G. M. Tielens, 239
- Tram, L. N. & Hoang, T. 2022, *Front. astron. space sci.*, 9, 923927
- Tram, L. N., Hoang, T., Lee, H., et al. 2021a, *ApJ*, 906, 115
- Tram, L. N., Hoang, T., Soam, A., Lesaffre, P., & Reach, W. T. 2020, *ApJ*, 893, 138
- Tram, L. N., Hoang, T., Wiesemeyer, H., et al. 2024, *arXiv e-prints*, arXiv:2403.17088
- Tram, L. N., Lee, H., Hoang, T., et al. 2021b, *ApJ*, 908, 159
- Truong, B. & Hoang, T. 2024, *arXiv e-prints*, arXiv:2407.14896
- Vaillancourt, J. E., Andersson, B. G., Clemens, D. P., et al. 2020, *ApJ*, 905, 157
- van Holstein, R. G., Stolker, T., Jensen-Clem, R., et al. 2021, *A&A*, 647, A21
- Weintraub, D. A., Goodman, A. A., & Akeson, R. L. 2000, in *Protostars and Planets IV*, ed. V. Mannings, A. P. Boss, & S. S. Russell, 247–272
- Whittet, D. C. B., Hough, J. H., Lazarian, A., & Hoang, T. 2008, *ApJ*, 674, 304
- Whitworth, A. P. & Ward-Thompson, D. 2001, *ApJ*, 547, 317
- Wright, C. M., Aitken, D. K., Smith, C. H., Roche, P. F., & Laureijs, R. J. 2002, in *The Origin of Stars and Planets: The VLT View*, ed. J. F. Alves & M. J. McCaughrean, 85